A Vector Model of Adiabatic Decoupling

Thomas E. Skinner* and M. Robin Bendall†

*Physics Department, Wright State University, Dayton, Ohio 45435, and †Russell Grimwade School of Biochemistry and Molecular Biology,
University of Melbourne, Parkville 3052, Victoria, Australia

A vector model of adiabatic decoupling is enunciated for an IS-coupled system of two spin-$\frac{1}{2}$ heteronuclei in the high-power limit of ideal adiabatic pulses. The observed S-spin magnetization evolves according to a time-dependent coupling that scales as the z component of an I-spin vector which evolves due to the applied decoupling irradiation. Simple analytical expressions are derived both on and off resonance for the reduced coupling during an ideal sech/tanh inversion pulse and for the resulting signal when either in-phase or antiphase magnetization is present at the start of decoupling. The resulting model allows one to readily envision decoupling experiments, make accurate estimates of sideband intensity, and assess the relative performance of different decoupling schemes. The utility of the model is further demonstrated by applying it to several recently proposed methods for reducing sidebands. In the limit of ideal adiabatic pulses, the predictions of the vector model are almost identical to those of quantum mechanics. At the lower RF power levels used in practical adiabatic decoupling applications, where the pulses are no longer perfectly adiabatic, phase cycles are employed to achieve performance that approximates the ideal limits derived here, so the vector model is more generally applicable, as well. These limits establish standards for future determination of the most efficient parameters for practical applications of broadband adiabatic decoupling in a single transient. © 1998 Academic Press

Key Words: adiabatic decoupling; broadband decoupling; sidebands; vector precession.

INTRODUCTION

Quantum mechanics provides an unerringly accurate description of NMR phenomena. Given sufficient computational resources, the results of any NMR experiment can be calculated with precision. Although the theory needs no supporting visual model for its application, such models can provide significant insight into the evolving physical processes underlying the results of a rigorous calculation. Moreover, visualization can allow one to intuit correct results and predictions for new experiments "on-the-fly," a useful capability that is often precluded by a pure resort to the abstract machinery of quantum mechanics. Playing a role both complementary and supplementary to the theory, an intuitive approach may also elicit relevant new questions that can then be solved in detail, or impose reasonable values for parameters, approximations, or

logical boundary conditions as a starting point for a full calculation.

In this article, we develop a vector model of adiabatic decoupling. We employ the Heisenberg vector model (*1*), which provides an accurate method for visualizing and quantifying weakly coupled spin evolution in NMR. It is readily applied to the majority of NMR pulse sequences in which spin evolution during the pulse can be ignored, and is particularly simple to apply in the case of two coupled spin-$\frac{1}{2}$ heteronuclei I and S (*2, 3*). Recently, this picture was extended to include coupling evolution during an adiabatic pulse (*4*). We show that the new model provides significant insight into the functional details of an adiabatic decoupling sequence and clearly illustrates some of the advantages inherent in modulating RF amplitude/frequency using the sech/tanh (hyperbolic secant) pulse (*5*) for adiabatic decoupling (*6, 7*). We expect that the model will also clarify other situations of practical importance. For example, whereas asynchronous decoupling is useful when employed with composite pulses, it actually degrades the performance of adiabatic decoupling, as reported previously (*8*). The model provides a simple but accurate means of predicting the performance of this method and other proposed schemes for reducing sidebands.

The model also gives a straightforward mechanism for the production of coherence sidebands in adiabatic decoupling (*8–10*). Coherence sidebands are new in the sense that longitudinal and transverse coherence were generally considered to be undetectable in 1D spectra obtained with the decoupler on during acquisition. A quantum-mechanical derivation accounting for the existence of these RF-induced coherence signals is given in Eq. [2] of Ref. (*10*). A detailed treatment of related phenomena that were predicted to occur in 1D spectra only with the decoupler switched off during acquisition can be found in (*11*). The discussion therein also noted that effects could be expected in multidimensional spectra even with the decoupler on during acquisition. Examples can be found in (*12*) and (*13*).

An analytical expression for the time-dependent coupling operative during the sech/tanh pulse is derived in the limit of ideal adiabaticity. Simple closed-form solutions—applicable over the full decoupled bandwidth—are provided for the signal

resulting from various initial configurations of the magnetization at the start of decoupling. From these solutions, we calculate a greatest lower bound for the maximum sideband amplitude as a function of the relevant sech/tanh input parameters (which is to say, the maximum sideband cannot be less than this bound, but will be equal to it under ideal conditions). Since the intensity of the decoupled centerband depends sensitively on sideband amplitude, the analysis also sets an upper limit (least upper bound) on the intensity of the decoupled peak, which is an important factor in determining the signal-to-noise ratio of a given decoupling experiment. The vector model shows that these bounds are applicable off resonance, across the full effective decoupled bandwidth. These derived bounds provide useful limits for the performance of adiabatic decoupling in a single transient and set boundaries that help define a potentially superior method. Ultimately, phase cycles are implemented to approximate the performance represented by the ideal limits, so the picture provided by the vector model is relevant to the problems of real adiabatic decoupling as well.

THEORY

The intuitive vector model described in this section was not derived in the usual sense of the term, but a plausibility argument can be constructed that clarifies connections between the model and the exact quantum-mechanical treatment of adiabatic decoupling. First, an implementation of the sech/tanh inversion pulse is defined. A brief outline of the steps necessary to perform a complete quantum-mechanical calculation of adiabatic decoupling for a simple IS-coupled system of two spin-$\frac{1}{2}$ heteronuclei follows. The S spins are observed while the decoupling irradiation is applied to the I spins. From this overview, we identify a time-dependent coupling which can be related to the orientation of the effective field seen by the I spins. The necessity of accommodating different initial conditions at the start of decoupling, however, requires a more general picture of this coupling which we relate to the orientation of vectors associated with the I spins. The resulting model is summarized at the end of the section.

Adiabatic Decoupling and Quantum Mechanics

The time-dependent amplitude/frequency modulation functions of the sech/tanh pulse can be parameterized in a reference frame rotating at the instantaneous frequency of the pulse (i.e., the frequency-modulated (14) FM frame) as

$$\mathbf{B}_1 = RF_{max}\text{sech } \beta(1 - 2t/T_p)\hat{\mathbf{x}} \qquad [1]$$

$$\mathbf{\Delta H} = bwdth/2\left[\tanh \beta(1 - 2t/T_p) + s\right]\hat{\mathbf{z}}. \qquad [2]$$

RF_{max} is the maximum amplitude of the B_1 field, which defines the x axis in the FM frame. The inversion pulse length is T_p. The frequency is swept in the range $\pm bwdth/2$, appearing as

an additional field along the z axis in this frame, and s is the resonance offset of the pulse in units of $bwdth/2$, where $s = 0$ denotes on-resonance decoupling. A value $\beta = 5.3$ is typically chosen to truncate the exponential decay of the sech function at a value of 0.01. The total effective field B_e, which is the vector sum of the fields in Eqs. [1] and [2], thus begins aligned with the $+z$ axis to a high degree of approximation, then sweeps through the x axis at time $T_p/2$ for $s = 0$, and becomes aligned (approximately) with the $-z$ axis at the end of the pulse.

A formal solution for the results of a decoupling experiment applied to the I spins can be obtained by transforming to a coordinate frame rotating with B_e. In the weak-coupling limit, the Hamiltonian $\mathcal{H}$ is diagonal in this frame. The propagator between initial time t_0 and final time t is simply $\exp[-i\mathcal{H}(t - t_0)]$, and the solution for the state of the system can be transformed back to the laboratory frame in order to calculate the results of a measurement on the system. An example of this approach applied to the case of adiabatic polarization transfer can be found in (15), based on the formalism developed in (16) for treating coherence transfer in the rotating frame. Alternatively, in the FM frame, the interval $(t - t_0)$ can be divided into a sequence of subintervals which are sufficiently small that $\mathcal{H}$ is approximately constant during each increment. Propagating the evolution of states in this sequence of time-independent steps provides a solution at any time t, as in the general treatment of decoupling given in (17).

In the high-power limit where the pulse is sufficiently adiabatic that the I spins are spin-locked to the effective field, the theory admits a more visual interpretation that provides a detailed physical picture of adiabatic decoupling. We first recall some important differences between the present case, in which continuous RF irradiation is applied, and previous vector models of nuclear spin evolution. In situations involving only chemical-shift and coupling evolution, all terms in the Hamiltonian commute, so each effect can be treated separately. One can calculate the time evolution of either the operators (Heisenberg picture) or states (Schrödinger picture) and identify a clear correspondence with a classical vector rotating in the expected manner. When an RF field is applied orthogonal to the z axis, the terms in $\mathcal{H}$ no longer all commute, and the propagator due to coupling and the RF field must be treated as a single entity. Effects that are uniquely quantum phenomena can result from the noncommutation of the operators. The time evolution of operators or states can still be calculated, but the correspondence with a classical vector rotating in physical space is more difficult to discern, since the states themselves evolve in an abstract Hilbert space. The connection between this abstract space and real, physical space is maintained through the calculation of expectation values. Although classical reasoning can be applied to the expectation values (but not directly to the states), the quantum-mechanical result for a general decoupling experiment (10, 17) can be difficult to

interpret visually, and the equations in the case of specific experiments usually must be solved numerically.

Time-Dependent Coupling

As a first step in identifying a classical analog to decoupling theory, we consider the Hamiltonian in the frame rotating with B_e. The required transformations implicitly rotate the quantization axis of the I spins in the FM frame to the axis defined by the direction of B_e. In the adiabatic limit, the I spins will remain aligned with B_e as the orientation of B_e changes in the FM frame. For S-spin heteronuclei during irradiation of the I spins, $\Delta H \gg B_1$, and the effective field seen by the S spins is aligned with the z axis of the FM frame to a high degree of accuracy. Thus, with the polar angle θ giving the orientation of B_e with respect to the z axis, the coupling term $J_0 \, \mathbf{I} \cdot \mathbf{S} \approx J_0 (I_z \cos\theta) S_z$ in this frame (neglecting off-diagonal terms involving transverse operators in the weak coupling limit). This result is a particular case of more general derivations provided in Eq. [18] of Ref. (16) and Eq. [14] of Ref. (15) for RF irradiation applied to both the I and S spins.

The energy level differences that appear as line splitting are unaffected by the transformations between the various rotating frames just mentioned, and we therefore identify a time-dependent reduced coupling

$$J_r(t) = J_0 \cos\theta(t) \qquad [3]$$

valid in both the FM frame and the laboratory frame for the high power limit of adiabatic decoupling. This result, previously deduced and supported by intuitive arguments (but defined in terms of the angle between B_e and the transverse plane), has been verified experimentally (4).

In the adiabatic limit, where the system is in an eigenstate of the instantaneous Hamiltonian, we can derive the same result by diagonalizing the FM-frame Hamiltonian to obtain, similar to (18),

$$J_r = [(\Delta H + J_0/2)^2 + B_1^2]^{1/2} - [(\Delta H - J_0/2)^2 + B_1^2]^{1/2}, \qquad [4]$$

which we write in the form

$$\frac{J_r}{B_e} = \left[1 + \frac{(J_0/2)^2 + J_0\Delta H}{B_e^2}\right]^{1/2} - \left[1 + \frac{(J_0/2)^2 - J_0\Delta H}{B_e^2}\right]^{1/2}. \qquad [5]$$

For $B_e = [B_1^2 + (\Delta H)^2]^{1/2} \gg J_0$, which is a negligible restriction in many applications, expanding the radicals and keeping the first nonvanishing term gives

$$J_r \approx J_0\Delta H/B_e, \qquad [6]$$

for the magnitude of the reduced coupling, which is the same as Eq. [3], since $\cos\theta = \Delta H/B_e$.

Quantization Axes

The Hamiltonian and, hence, the time-development operator do not depend on the initial state of the system, but the outcome of a given experiment does. So far, there is nothing in the model that distinguishes between different initial conditions, on which the subsequent state of the system depends. The expression for the reduced coupling in $\mathcal{H}$ was obtained for the I spins implicitly quantized along B_e. On physical grounds, we expect the energy levels of an individual S spin coupled to an I spin in a magnetic field to depend on the orientation of the I spin in the field rather than on the orientation of the field itself. In the standard vector model of coupling evolution in the absence of RF irradiation, the coupling is represented by the semiclassical vectors I_α and I_β, antiphase along the z axis defined by the polarizing field, B_0. In the present model incorporating the influence of the RF field, a dependence on initial conditions arises if the coupling is related to the orientation of similar semiclassical vectors rather than the direction of B_e. The time evolution of the I vectors provides the necessary dynamics in the model, as described in the next section. We first consider how these I vectors are assigned in the model.

An NMR experiment begins with the spins in a $|\pm z\rangle$ state with respect to B_0. The small excess in the number of I spins in the ground state can be associated with a classical magnetization vector aligned with B_0. An applied RF field induces transitions between states to dynamically reorder the relative populations in a way that can be viewed as a vector precessing at the Larmor frequency about the effective field. But in a decoupling experiment that observes the S spins, the state of an individual I spin that is attached to an observable S-spin constituent of the sample determines the effect of the coupling. For in-phase S magnetization at the start of decoupling, there is no coherence between the I and S spins, and the corresponding state of the attached I spin might be considered to be indeterminate, in the sense that it has not been "measured." There is equal probability of the spin being in a $|\pm\rangle$ state with respect to any measurement axis. In the FM frame, this axis is established by B_e, as reflected in Eq. [3]. However, coherence between the I and S spins reveals the state of the attached I spin. For example, if the S spin evolves from a $|+x\rangle$ state to a $|\pm y\rangle$ state prior to decoupling, it was attached to a $|\mp z\rangle$ I spin. The state of the I spin has been "measured," so, in this case, there is a preferred direction established, prior to and independent of B_e. The I spins have been ordered along the z axis, and subsequent pulses, in particular the applied decoupler irradiation, can convert this to order along the x or y axes.

The Vector Model

We therefore employ a modified standard coupling model using the semiclassical vectors I_α and I_β to describe ideal

RF_{max} (kHz)	Experimental				Predicted				$bwdth/(RF_{max})^2$
	$1/T_p$	$2/T_p$	$3/T_p$	$4/T_p$	$1/T_p$	$2/T_p$	$3/T_p$	$4/T_p$	
9.9	0.53	−0.12	0.05	−0.02	0.54	−0.12	0.05	−0.02	0.5
6.8	0.54	−0.13	0.06	−0.03	0.55	−0.13	0.05	−0.03	1.0
6.0	0.54	−0.13	0.06	−0.03	0.55	−0.13	0.05	−0.03	1.3

^{a} The high-power limit in sech/tanh decoupling, where phase cycling has no effect on the intensity of sidebands, is nominally $bwdth/(RF_{max})^2 \lesssim 0.5$ (*20*). At lower power, phase cycles used in adiabatic decoupling generate additional sidebands at the cycling frequency and its harmonics, but have little effect on n/T_p sidebands, as discussed in the "On-Resonance Decoupling" section of the text.

adiabatic decoupling, in which the observed magnetization is determined by associated vectors S_α and S_β that precess in opposite directions in the transverse plane at a time-dependent frequency $J_r/2$ instead of a constant $J_0/2$. The projection of I_α on the z axis defines the instantaneous reduced coupling

$$J_r(t) = J_0 \left[I_\alpha(t) \right]_z \qquad [7]$$

for unit vector I_α. For in-phase S magnetization at the start of decoupling, the I vectors are aligned with B_e. If there is order between the I and S spins prior to application of the decoupling irradiation (e.g., $S_y I_j$, with $j = x$, y, or z), this coherence establishes a preferred orientation for the I spins given by the direction of I_j. If the decoupler field is applied at an angle to this axis, the I vectors will precess about the field in the usual manner and affect the instantaneous coupling accordingly.

For most cases of interest in adiabatic decoupling, the direction of B_e coincides with I_α. We present quantitative results of the vector model applied to these cases. We also show that the vector model readily explains differences in the nature of the signal produced by transverse coherence compared to longitudinal coherence at the start of decoupling. A quantitative treatment of decoupling applied to transverse coherence, where the I-vectors are not aligned with B_e, further illustrates the power and utility of the model.

EXPERIMENTAL

Experimental spectra used in the quantification of sidebands were obtained from ^{1}H-detected ^{13}C-decoupled spectra (16 transients) generated from the heteronuclear spin-echo difference pulse sequence (*19*) followed by STUD+ decoupling (*8*) using a sample of ^{13}CH$_3$I (2% in CDCl$_3$, with 0.2% Cr(AcAc)$_3$ relaxation agent; $J_{CH} = 150$ Hz) in a 5 mm HCN triple-resonance PFG probe on a 500 MHz Varian INOVA spectrometer. These spectra were obtained with the *bwdth* parameter set to 50 kHz, and each sech/tanh waveform in the STUD+ pattern was delivered as 500 increments of RF amplitude and

phase. RF amplitudes (RF_{max}) were calibrated by determining the 180° on-resonance pulse time for ^{13}C and are expressed as the reciprocal of the 360° pulse time in units of kilohertz.

The natural linewidth of the ^{1}H resonance of the sample was 2.6 Hz at half height and this was exponentially line broadened to approximately 4 Hz. All spectra were baseline corrected using a spline fit (standard Varian NMR software) so that baseline regions either side of the centerband and each sideband were set to zero amplitude. All sideband amplitudes are the average of both sidebands on opposite sides of the centerband. These amplitudes were measured as peak heights relative to the centerband, assumed to be 100%. Under conditions of high RF decoupling power, sample heating induces variable linewidths, and it is not possible to exactly determine absolute centerband amplitudes experimentally. The relative measures were converted to absolute from the reduction of the centerband below 100% estimated from theoretical simulations. For the results presented this is a small correction, reducing a sideband amplitude of 0.56% to 0.53% as in Table 1, for example, and the $1/(2T_p)$ sideband of 2.05%, relative, described in the "Asynchronous Decoupling" section, to an absolute value of 1.98%. Thus, all sideband levels are quoted as percent absolute to facilitate the comparison of experimental and theoretical results.

Measurement of the dispersion-mode $1/(2T_p)$ sideband described in the "Misset J-Delay Periods" section presented a more difficult problem. Phase correction by 90° allows measurement of the amplitude, but the resulting large dispersion-mode wings on the centerband introduces ambiguity into the baseline around the sidebands. Alternatively, measurement of the sidebands relative to the centerband in an absolute-value spectrum also introduces baseline ambiguity because all signals are broadened. The quoted value of 9.1% absolute is an average of 8.9% and 9.3%, respectively, from these two methods.

Signals measured from transverse coherence during decoupling (plotted in Fig. 5) were acquired after application of the pulse sequence

$$90_x[H]-1/(4J)-\{180[H], 180[C]\}$$

$$-1/(4J)-90_y[H]-G-\{90[H], 90[C]\}$$

to prepare the pure antiphase state S_yI_x. G is a short pulsed-field gradient to suppress unwanted transverse ^1H magnetization. The phases of the final 90[H], 90[C] pulses and the STUD waveform were alternated in conjunction with the receiver phase to reduce experimental artifacts. Two separate spectra were obtained, one with a 90° phase for the first pulse in the STUD train (Fig. 5a), and a second with zero phase (Fig. 5b). A total of 4096 transients were accumulated and the real FID is displayed after phase correction so that no signal is present in the imaginary FID. The FIDs were digitized in 10 μs steps.

APPLICATIONS

On-Resonance Decoupling

For in-phase S magnetization at the start of on-resonance decoupling ($s = 0$), the system evolves as depicted in Figs. 1a–1c. The I vectors are aligned with B_e along the z axis at the beginning of the first adiabatic inversion pulse, and $J_r(0) = J_0$. During the pulse, the two S-spin vectors precess in opposite directions in the transverse plane at an instantaneous frequency $J_r/2$ relative to the center, or average, frequency of the two lines, reverse direction at time $T_p/2$ when J_r changes sign, and refocus at time T_p. The detected signal relative to this center frequency is $\cos\varphi(t)$, where the time-dependent precession angle $\varphi(t)$ in the transverse plane, as illustrated in Figs. 1a–1c, is obtained as the integral of the angular frequency, $\pi J_r(t)$. For the second inversion pulse, shown in Fig. 1c, the labels of the spin vectors are exchanged compared to the first pulse, so $\varphi \rightarrow -\varphi$ during this period. Thus, φ (and α, below) is an odd function with period $2T_p$, whereas the signal $\cos\varphi(t)$ is an even function with period T_p.

As a bookkeeping device enabling a concise expression for $\varphi(t)$, valid for all t, we define k as the quotient t/T_p rounded to the lowest integer. Starting with $k = 0$, the time interval between kT_p and $(k + 1)T_p$ is counted as the kth interval. We also define t_k as $t - kT_p$, so $0 \leq t_k \leq T_p$. Then, on resonance, we obtain

$$\varphi(t) = \pi J_0\alpha(t)T_p/2, \qquad [8]$$

where

$$\alpha(t) = \frac{(-1)^k}{\beta}\left\{\cosh^{-1}\left[\frac{\cosh\beta}{\sqrt{1-v^2}}\right] - \cosh^{-1}\left[\frac{\cosh\beta(1-2t_k/T_p)}{\sqrt{1-v^2}}\right]\right\}[9]$$

with v defined as $RF_{max}/(bwdth/2)$. More simply, the function $\alpha(t)$ is constructed using the time interval $[0, T_p]$ and is repeated with alternating sign in subsequent intervals. Details

of the derivation are provided in the Appendix. The maximum precession of the S spins, depicted in Fig. 1b, is given by $\pi \bar{J}T_p/2$, where the average coupling during the time $T_p/2$ is

$$\bar{J} = J_0 \, \alpha(T_p/2). \qquad [10]$$

Specific values for $\bar{J}$ have previously been obtained by numerical integration (4), in agreement with the explicit results of Eqs. [8] and [9].

Sideband intensity. In the complete absence of coupling, the S-spin signal detected on resonance would be constant, which we normalize to one to simplify the discussion. As demonstrated in Figs. 1a–1c, however, some coupling precession and refocusing of the S vectors must occur during each adiabatic decoupling pulse, because the pulse cannot be instantaneous. The maximum precession angle, which determines the amplitude of the resulting signal modulation, will increase with T_p. For ideal inversions, as in the high power adiabatic limit (e.g., $bwdth/(RF_{max})^2 \lesssim 0.5$ for sech/tanh pulses) the form of this modulation is repeated exactly throughout the entire train of decoupling pulses with a period equal to T_p. If the modulation could be described as a simple sinusoid, $A\cos(2\pi t/T_p)$, which is added to the constant DC component of the on-resonance signal, $(1 - A)$, the Fourier transform of the S signal would produce the centerband and sidebands at $\pm 1/T_p$ relative to the centerband. The actual signal is $\cos\varphi(t)$, using Eq. [8]. It is not a simple sinusoid, but consists of the fundamental frequency $1/T_p$, which determines the period of the oscillation, and higher frequency components, which characterize the departure of the modulation from a single sinusoid. The Fourier transform of this signal gives the decoupled center peak and sidebands at integer multiples of the fundamental frequency. These are the only sidebands that appear under these ideal conditions. Phase cycling the train of adiabatic pulses at lower power in typical decoupling applications is designed to compensate for imperfect inversions by achieving approximately ideal inversions over periods mT_p, resulting in additional sidebands at $1/(mT_p)$ and its harmonics. These phase cycles should therefore have little or no effect on n/T_p sidebands. This can be seen in Fig. 3 of Ref. 8, where the maximum sideband amplitude at high RF power, which appears at $1/T_p$, is the same independent of the phase-cycling scheme used. Further confirmation is provided in Table 1, where the n/T_p experimental sideband amplitudes for STUD+ on resonance are almost identical to those calculated from the Fourier transform of $\cos\varphi(t)$, independent of RF power.

Thus, in the high power limit, on resonance, the vector model of a single adiabatic pulse provides an accurate description of adiabatic decoupling. For the sech/tanh pulse, we will show later that the intensity of the $1/T_p$ sideband on resonance sets the lower bound on the maximum sideband amplitude over the full decoupled bandwidth in the adiabatic limit. Similarly, the centerband sets the upper bound on the intensity of the
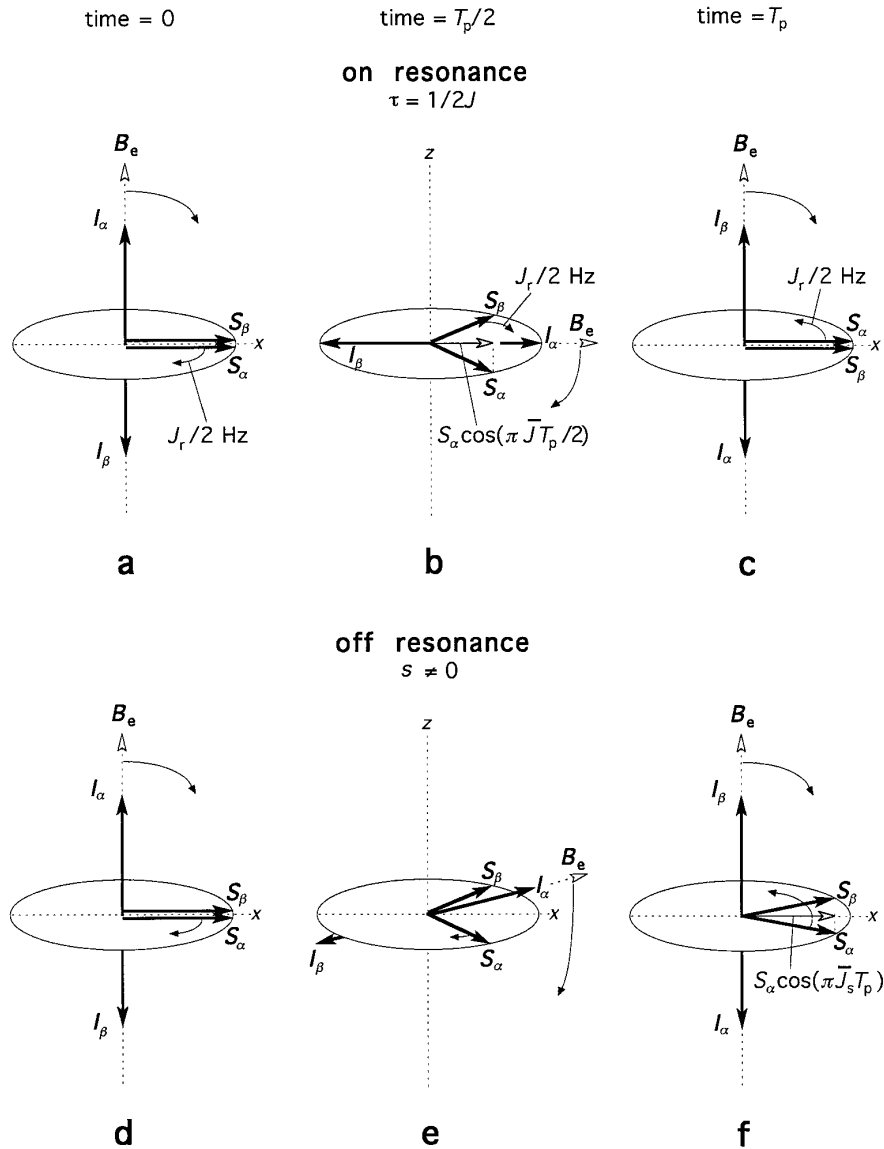
time = 0   time = $T_p/2$ time = T_p

on resonance
$\tau = 1/2J$

a   b   c

off resonance
$s \neq 0$

d   e   f

FIG. 1. (a) After an ideal pulse sequence, just preceding signal acquisition ($t = 0$), the S signal will be focused in the transverse plane. At the beginning of the first adiabatic decoupling pulse, the effective field, B_e, is aligned with the $+z$ axis. With no coherence between I and S, this determines the quantization axis of the I spins, which have an equal probability of being along $\pm z$. The S magnetization can thus be divided into two coincident vectors, with their associated I vectors antiphase along the z axis. During the adiabatic pulse, B_e rotates through the x axis to $-z$. Provided the adiabatic condition applies, the I vectors rotate with B_e. In addition, the S vectors precess in the transverse plane at a rate proportional to the z-axis components of I_α and I_β. The time-dependent reduced coupling J_r is given by Eqs. [3] and [7], and the time-dependent precession angle derived from this is given in Eqs. [8] and [9]. At the beginning of the pulse, the S vectors precess at an instantaneous frequency $J_0/2$ Hz, where J_0 is the normal coupling constant. This rate of precession decreases to zero as I_α and I_β pass through the transverse plane. (b) For on-resonance decoupling ($s = 0$), at the midpoint of the pulse, time $t = T_p/2$, the S vectors will be stationary and will have precessed through their maximum angle given by $\pi \bar{J} T_p/2$, where $\bar{J}/2$ is the average rate of precession during half of the pulse, given by Eq. [10]. During the second half of the pulse the S precession is in the reverse direction, again at the average rate of $\bar{J}/2$. (c) The spins at the start of the second decoupling pulse have refocused along the x axis at time $t = T_p$. This cycle repeats every T_p, modulating the total S signal with a period of T_p and generating sidebands at the fundamental frequency $\pm 1/T_p$ and its harmonics. (d) For off-resonance decoupling the vector picture begins as for on-resonance decoupling in Fig. 1a. (e) If the offset parameter, s, is positive, B_e and the I spins will not have rotated completely to the transverse plane at the midpoint of the pulse, $t = T_p/2$, and the precession of the S spins continues at a decreasing rate until the I spins are transverse, where the coupling is zero. During the second half of the pulse, B_e and the I spin vectors pass through the transverse plane, and the S precession reverses. (f) At $t = T_p$ the S spins have not quite refocused and make an angle, $\pi \bar{J}_s T_p$, with respect to the x axis, where $\bar{J}_s/2$ is the average rate of precession for the entire pulse given by Eq. [13]. During a second adiabatic pulse this net precession angle is accumulated in the opposite direction, and the S spins refocus with an overall cycle time of $2T_p$, generating sidebands at $\pm 1/(2T_p)$ and its harmonics. (g) If the τ delay time in a heteronuclear spin-echo experiment is misset at $1/(4J)$ or $3/(4J)$, the S vectors for odd transients will be antiphase along the y axis just prior to decoupling. The coherence represented by the ordered $S_y I_z$ state establishes a preferred orientation for the I spins, which are antiphase along the z axis. Some antiphase S magnetization will exist for any $\tau \neq 1/(2J)$, or for any other preparation pulse sequence where nonideal $n/(4J)$ delays must be used.
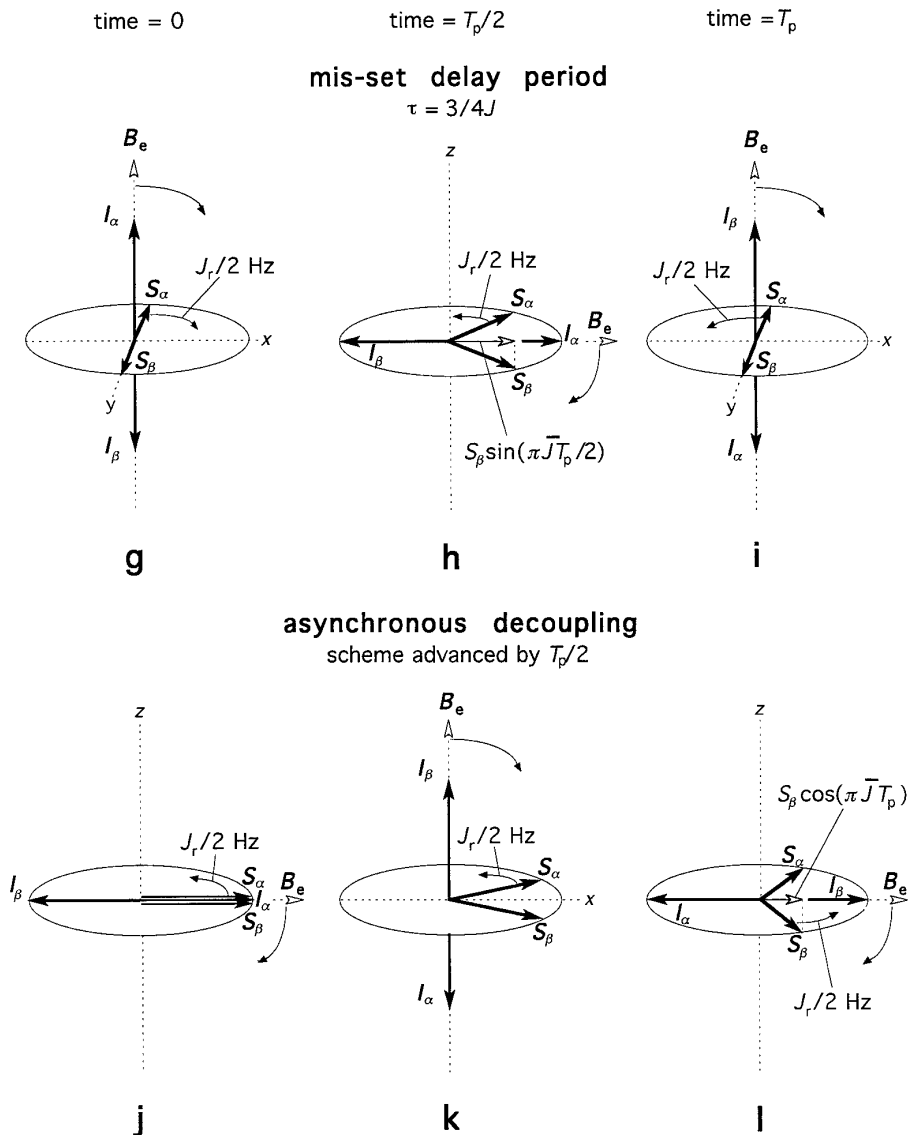
mis-set delay period
$\tau = 3/4J$

g   h   i

asynchronous decoupling
scheme advanced by $T_p/2$

j   k   l

FIG. 1—*Continued*

decoupled central peak, which determines the signal-to-noise performance of sech/tanh decoupling. Centerband and sideband amplitudes are obtained from the Fourier transform of cos $\varphi(t)$ and are plotted in Fig. 2 (solid lines) as a function of T_p for $bwdth = 50$ kHz and a high power limit of $bwdth/(RF_{max})^2 = 0.1$. Previous extensive plots of experimental sideband calibration curves (20) for a range of $bwdth$ values (5–120 kHz) show that this value for $bwdth/(RF_{max})^2$ is sig-

---

(**h**) At $t = T_p/2$, the S vectors will have precessed through the same maximum angle as in Fig. 1b. (**i**) At $t = T_p$, the S vectors will have returned to their initial state, similar to Fig. 1c. However, unlike the example shown in Fig. 1c, the two S vectors are antiphase along the y axis, so they precess in the opposite direction in the transverse plane during a second pulse of period T_p, modulating the total S signal with a period of $2T_p$ and producing sidebands at $\pm 1/(2T_p)$ and its harmonics. (**j**) For in-phase S magnetization, if an on-resonance decoupling scheme is begun halfway through an adiabatic pulse, the effective field establishes the quantization axis of the I spins, which have an equal probability of being along $\pm B_e$. The initial S magnetization can be divided into two coincident vectors, associated with the corresponding antiphase I vectors, and these S vectors will precess at an average rate of $\bar{J}/2$ during the first $T_p/2$ period. (**k**) At $t = T_p/2$ the S precession will continue in the same direction at the same average rate as the second adiabatic inversion pulse is initiated. (**l**) At $t = T_p$, the S vectors will have precessed twice as far as in Fig. 1b and make an angle, $\pi \bar{J} T_p$, with respect to the x axis. The S vectors are stationary at this time; then, since the z component of I_α becomes positive, they reverse their precession and refocus during a second cycle of period T_p. Complete refocusing occurs every $2T_p$, thus generating sidebands at $\pm 1/(2T_p)$ and its harmonics.
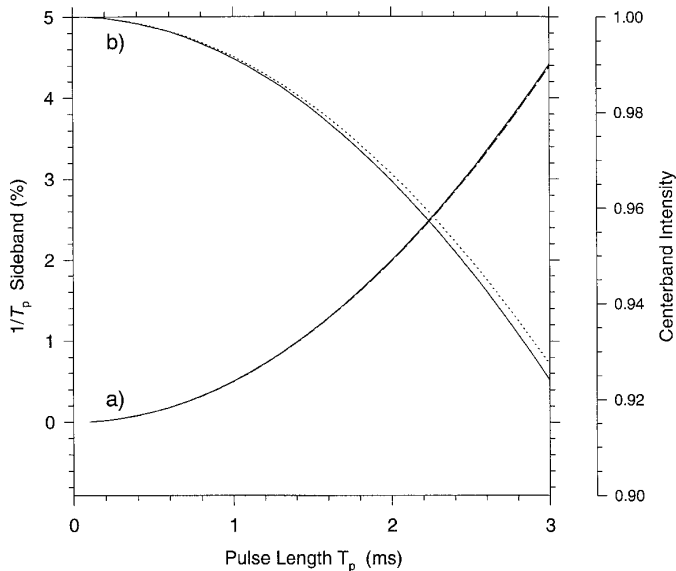
FIG. 2. (a) Solid line: Absolute intensity of the $1/T_p$ sideband, relative to a fully decoupled central peak height of 1, for on-resonance decoupling in the high-power limit of ideal adiabaticity, plotted as a function of the length, T_p, of a single inversion pulse. The plotted values were obtained by Fourier transforming the exact vector-model signal $\cos\varphi(t)$ from Eqs. [7] and [8] ($bwdth/(RF_{max})^2 = 0.1$, $bwdth = 50$ kHz, $J_0 = 150$ Hz), using the time-dependent coupling $J_r(t)$ as derived in the Appendix. This curve is indistinguishable from the result of an exact quantum-mechanical calculation. Relative intensity can be obtained by dividing these values by the central peak heights provided in part (b) by the scale on the right. Dashed line: $1/T_p$ sideband intensity using Eq. [11] ($n = 1$), obtained by approximating the exact vector model signal as $\cos(\pi\bar{J}t)$, where $\bar{J}$ is the average on-resonance coupling during time $T_p/2$. The precessing spins reverse direction at $T_p/2$ and refocus at T_p, so the average on-resonance coupling during the entire pulse is zero. The value $bwdth/(RF_{max})^2 = 0.7$ was used to compensate for the effects of substituting a constant $\bar{J}$ in place of the true time-dependent coupling, as described in the text. (b) Solid line: Centerband intensity obtained from exact vector-model signal, as above. Dotted line: Centerband intensity obtained from $\cos(\pi\bar{J}t)$, as above.

nificantly below the level where sideband intensity becomes insensitive to further increases in RF power, indicating the limit of ideal adiabaticity has been reached.

A simple estimate of the $1/T_p$ sideband can also be obtained from the amplitude of the $\cos\varphi(t)$ modulation of the S-spin FID, although this clearly ignores the presence of higher frequency components due to both the abrupt change in precession of S_α and S_β at time $T_p/2$ and the fact that the precession frequency is not constant. Half the peak-to-peak amplitude of the modulation on a scale where the central peak from the two S-spin vectors is normalized to one (i.e., another factor of $\frac{1}{2}$) gives[1] $0.25[1 - \cos(\pi\bar{J}T_p/2)]$ for the intensity of the $1/T_p$ sideband. This expression overestimates the actual maximum sideband amplitude given in Fig. 2 by $\sim 37\%$ for all T_p in the range 0.1 to 3 ms, but it serves to illustrate that a modulation with a simple period of T_p, in which the signal refocuses only

[1] In Ref. 8, this formula was erroneously typeset as $0.25 \cos(1 - \pi\bar{J}T_p/2)$.

at integral multiples of this period, must produce the largest sideband at $1/T_p$ even if the form of the modulation is more complicated than a single sinusoid.

Sidebands have also been estimated by assuming a constant value for the coupling J_0 during an inversion pulse (6) to obtain the result for standard spin-flip decoupling with ideal delta-function inversion pulses (21). The Fourier coefficients of this signal (a cosine arc reflected about $T_p/2$, giving a cusp at the midpoint of the pulse) also overestimate the maximum sideband in sech/tanh decoupling by $\sim 11\%$ over the same range of variation in T_p given earlier and overestimate the higher order sidebands by increasing amounts.

However, the present vector model shows why assuming constant J_0 for the spin evolution works reasonably well for sech/tanh decoupling. This particular amplitude/frequency modulation scheme keeps B_e (and therefore, I_α) closely aligned with the z axis for a significant fraction of the pulse, giving $J_r \approx J_0$ during these times, by Eq. [7]. We can tailor the estimate for sideband intensity given in Ref. (6) more specifically to sech/tanh decoupling by using the average coupling, $\bar{J}$, instead of J_0, to find the Fourier coefficients of the even function $\cos(\pi\bar{J}t)$ evaluated between $\pm T_p/2$ and expanded in terms of the basis set $\cos(2\pi nt/T_p)$. The signal intensity at n/T_p in the frequency domain is half the coefficient of the associated cosine term. We write our answer in the form given in (6) to obtain the modified result

$$A_n = \frac{1}{2}\left[\text{sinc}(n - \bar{J}T_p/2) + \text{sinc}(n + \bar{J}T_p/2)\right] \quad [11]$$

for the amplitude of the sideband at frequency n/T_p. The sinc-function dependence shows immediately that sidebands become progressively and rapidly smaller as a function of increasing order n. The sign of the sidebands is $(-1)^{n+1}$ for $n \neq 0$, which can be obtained by writing the foregoing $\text{sinc}(x)$ terms in the form $\sin(\pi x)/(\pi x)$. The centerband ($n = 0$) and maximum sideband ($n = 1$) amplitudes obtained using the approximation of Eq. [11] are plotted in Fig. 2 for comparison with the exact results. Using a constant $\bar{J}$ to obtain a signal $\cos(\pi\bar{J}t)$ in place of $\cos\varphi(t)$, derived in Eq. [8] from the true time-dependent coupling, again increases the amplitude of the higher frequency components due to the abrupt change in the cosine function at $T_p/2$, where refocusing begins, and results in a slight underestimate of the centerband and first sideband. To compensate, $bwdth/(RF_{max})^2 = 0.7$ was used to calculate $\bar{J}$, giving a better representation of the true signal that depends on variable $J_r(t)$.

Off-Resonance Decoupling

The time- and frequency-domain signals obtained using sech/tanh decoupling on resonance in the adiabatic limit can be obtained using Eqs. [8], [9], and [11]. An analogous, but more complicated, analytical expression can be derived for off-resonance decoupling ($s \neq 0$), as described in the Appendix,

and we have used this expression to verify that the $1/T_p$ sideband on resonance is the maximum sideband over the full decoupled bandwidth in the high-power limit of sech/tanh decoupling.

However, the salient features can be obtained more simply by noting that Eq. [2] gives $\Delta H = 0$ (i.e., B_e in the transverse plane) for

$$t = \frac{T_p}{2}\left[1 + \frac{\tanh^{-1}(s)}{\beta} \right], \qquad [12]$$

which occurs before (after) the midpoint of the pulse for negative (positive) offset s. Thus, B_e in off-resonance decoupling does not spend equal time above and below the transverse plane during a single pulse of length T_p. For negative offset s, the S spins refocus along the x axis at twice the time given in Eq. [12], and subtracting this from T_p gives a time T_p/β $\tanh^{-1}(s)$ at the end of the pulse during which unrefocused J evolution occurs. If the offset is positive, this period establishes a net separation for the S spins at the beginning of the pulse, then the spins precess further, reverse direction, and refocus to this separation at the end of the pulse. For the sech/tanh pulse, B_e is aligned, to a good approximation, with the $\pm z$ axis during this period of net J evolution, with the sign depending on the sign of s. We can therefore identify an average off-resonance coupling constant during the time T_p as

$$\bar{J}_s = (J_0/\beta)\tanh^{-1}(s). \qquad [13]$$

The same equation has been previously determined for the use of a single sech/tanh pulse at the center of a chemical-shift-correlation delay (4).

The situation is illustrated in Figs. 1d–1f for positive offset, s, where B_e crosses the transverse plane after the midpoint of the pulse. The period of unrefocused J modulation occurs at the beginning of the pulse when I_α is along $+z$. The resulting signal is shown in Fig. 3, calculated for a resonance offset of $s = 0.7$ in the high-power limit of sech/tanh decoupling. Partial refocusing occurs after the midpoint of the pulse, when B_e rotates I_α through the transverse plane, as depicted within the dotted lines in Fig. 3. The detectable fraction of S magnetization at the end of the pulse is $\cos(\pi \bar{J}_s T_p)$. Repetition of the pulse, with I_α now initially along $-z$, causes precession in the opposite orientation during the period of net J evolution ($\bar{J}_s$ of opposite sign during the second T_p) and leads to S_α and S_β being refocused in the transverse plane at the end of the second pulse. Therefore, the modulation for off-resonance decoupling is an even function with a period equal to $2T_p$.

Sideband intensity. As discussed earlier, the on-resonance time-domain signal is an even function with period T_p and can be decomposed as a linear combination of cosine terms of frequency n/T_p, leading to Eq. [11] for the intensities of the
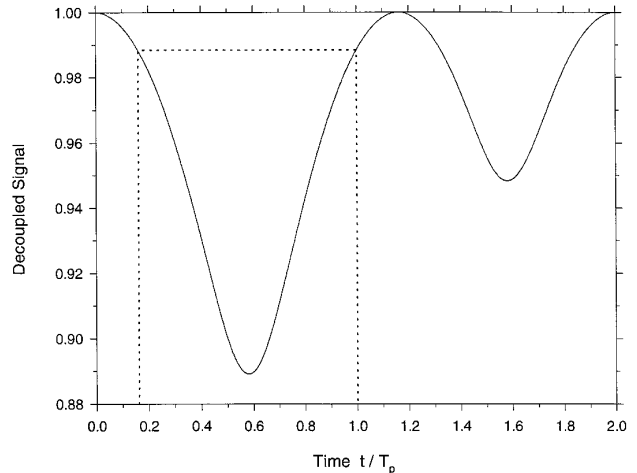

FIG. 3. The off-resonance ($s = 0.7$) decoupled signal $\cos\varphi(t)$ derived from the vector model is plotted as a function of time t/T_p, normalized to the pulse length, in the high-power limit of sech/tanh decoupling using parameters $(bwdth/(RF_{max})^2 = 0.1$, $bwdth = 50$ kHz, $T_p = 2$ ms for a coupling $J_0 = 150$ Hz. The off-resonance precession angle $\varphi(t)$ in the transverse plane is derived in the Appendix and is indistinguishable, in the high-power limit used here, from the result of an exact quantum-mechanical calculation. As illustrated in Figs. 1d–1f and described in the text, the S magnetization vectors precess apart for a time $(T_p/\beta) \tanh^{-1}(s)$ at the beginning of the pulse, continue to separate until the effective field rotates I_α through the transverse plane after the midpoint of the pulse, as given in Eq. [12], then partially refocus during the remainder of the pulse. This period during which there is no net precession is delineated by the dotted lines in the figure. The net precession angle at $t = T_p$ is thus established at the beginning of the pulse. During a second adiabatic pulse, this net precession angle is accumulated in the opposite direction, as shown above for $t/T_p > 1$, and the S spins refocus with an overall cycle time of $2T_p$, generating sidebands at $\pm 1/(2T_p)$ and its harmonics. The unrefocused period at the beginning of the pulse is a small fraction of T_p for $|s| \lesssim 1$, giving small $1/(2T_p)$ sidebands over the full decoupled bandwidth. By contrast, for adiabatic decoupling schemes using linear frequency sweeps, the period of unrefocused modulation as a fraction of T_p is directly proportional to offset (see text). The amplitude of the modulation increases accordingly, and the intensity of the $1/(2T_p)$ sideband therefore has a strong dependence on the resonance offset of the decoupler for a linear frequency sweep.

centerband and sidebands. To assess the changes that occur in sideband intensities off resonance, we consider what must occur if the decoupler is offset from resonance by an infinitesimal amount. The Fourier-series expansion of the signal must now include an infinitesimally small term of frequency $1/(2T_p)$ to shift the period to $2T_p$, and the coefficient of the $1/T_p$ term must be correspondingly decreased so the signal amplitude remains unchanged at $t = 0$. As the decoupler is moved farther off resonance, the amplitude of the $1/(2T_p)$ component continues to increase, while the amplitude of the $1/T_p$ term decreases accordingly. However, as reported previously (4), Eq. [12] for sech/tanh decoupling is relatively insensitive to offset for $|s| \lesssim 1$, resulting in a weak dependence of the $1/(2T_p)$ sidebands on s, since B_e crosses the transverse plane near the midpoint of the pulse for a large fraction of the decoupled bandwidth (for example, at $t/T_p = 0.55$, 0.60, 0.64, and 0.67 for $s = 0.5$, 0.8, 0.9, and 0.95, respectively). Thus,

off resonance, the $1/(2T_p)$ sideband is less than the $1/T_p$ sideband, which, in turn, is less than the on-resonance $1/T_p$ sideband, over a large fraction of $bwdth$. The effective decoupled bandwidth in our criterion for the quality of decoupling (20) is determined by the maximum sideband amplitude within the decoupled bandwidth. The $1/(2T_p)$ sidebands, which are produced only off resonance, will limit the effective bandwidth when they exceed the magnitude of the on-resonance $1/T_p$ sideband. To a good approximation, this will occur for s determined by the inequality

$$\cos(\pi \bar{J}_s T_p) \le \cos(\pi \bar{J} T_p / 2). \qquad [14]$$

Substituting Eq. [13] for $\bar{J}_s$ gives

$$|s| \ge \tanh\left(\frac{\beta \bar{J}}{2 J_0}\right). \qquad [15]$$

Values for $\bar{J}$ in the high power limit are typically greater than $0.9 J_0$, so the amplitude of the $1/(2T_p)$ sideband will be less than the amplitude of the $1/T_p$ sideband obtained on resonance for $|s| < 0.98$, by Eq. [15].

Offsets $|s| > 0.98$ exceed the normal STUD decoupled bandwidth, in which the centerband is within at least 80% of the central peak height for on-resonance decoupling, so the $1/(2T_p)$ sidebands generated off resonance by sech/tanh decoupling are not a limitation on its performance. The frequency selectivity of adiabatic pulses results from the violation of the adiabatic condition near offsets $s = \pm 1$, where the effective field is zero at the beginning or end of the pulse, by Eq. [2]. The effective bandwidth is determined by this violation and, as a fraction of the parameter $bwdth$ for STUD, typical experimental results show increases in effective bandwidth from 0.91 at $bwdth = 50$ kHz to 0.95 at $bwdth = 100$ kHz and close to 0.98 at $bwdth = 500$ kHz (9, 20). The phase cycling schemes of Ref. (8) are designed to compensate for the loss of adiabaticity and have very little effect on the intensities of n/T_p sidebands, as discussed earlier for the on-resonance case. However, new sidebands are introduced at $1/(mT_p)$, the cycling frequency of the phase cycle (usually $m = 5$, 10, or 20). Experimentally, the effective bandwidth is observed to be limited by the rapid increase in amplitude of one or more of the $1/(mT_p)$ sidebands above the magnitude of the on-resonance $1/T_p$ sideband, which can be determined from Eq. [11]. Thus, Eq. [11] determines the maximum sideband amplitude over the effective decoupled bandwidth in the high power limit of sech/tanh decoupling.

Sidebands in linear frequency sweeps. The prediction of modest $1/(2T_p)$ sidebands in sech/tanh decoupling is consistent with all experimental results. For example, such sidebands can be observed in Fig. 1c of Ref. (9) to be close to zero at the middle of the bandwidth, increasing moderately toward the edges of the bandwidth without ever exceeding the maximum sideband in the spectrum. By contrast, the S-signal modulation

that occurs off resonance when using a linear frequency sweep in an adiabatic decoupling scheme (22, 23) is easily seen to be more problematic. In this case, B_e will reach the transverse plane at time $t = (1 + s)T_p/2$, so that the period of unrefocused modulation increases linearly with offset. The amplitude of the modulation increases accordingly, and the intensity of the $1/(2T_p)$ sideband therefore has a strong dependence on the resonance offset of the decoupler. Although $\bar{J}$, which is applicable on resonance in the high-power limit, will be somewhat smaller relative to the value obtained using the sech/tanh pulse, the sideband performance of a linear frequency sweep over the full decoupled bandwidth is limited by the increasingly large $1/(2T_p)$ sideband off resonance (e.g., Fig. 1 of Ref. (9)). Other decoupling schemes employing amplitude/frequency functions that are constrained in a manner which improves adiabaticity off resonance for a chosen amplitude function (24, 25) give correspondingly better sideband performance, but we have not found any in our investigations to date that achieve sidebands as low as the sech/tanh pulse does for a given total decoupled bandwidth at the same average RF power (9).

Misset J-Delay Periods

Coherence sidebands (10) result from the presence, at the beginning of an adiabatic decoupling sequence, of either longitudinal or transverse coherence in the spins that are being observed. They are generated even in simple 1D decoupled spectra, in contrast to previously discovered coherence effects (11). Coherence sidebands are up to an order of magnitude larger than the sidebands produced by in-phase magnetization, and sidebands resulting from longitudinal coherence were demonstrated to be greater than those produced by transverse coherence. Antiphase magnetization is an unavoidable result in many useful preparation pulse sequences applied to realistic samples containing a range of J values. The associated coherence sidebands can be sufficiently large to render adiabatic decoupling impractical in many applications if they are not suppressed. In a previous communication (10), we devised several methods for eliminating these sidebands over decoupled bandwidths of up to 100 kHz, and, using a standard quantum mechanical calculation, derived an expression that can be solved numerically to determine their intensity. Space limitations precluded a description of the vector model, but it provides an accurate and more easily accessible estimate for the magnitude of coherence sidebands in sech/tanh decoupling, as well as significant physical insight into the mechanism of their production, leading to effective strategies for eliminating them.

Longitudinal coherence. In the heteronuclear spin-echo difference experiment, for odd transients just prior to decoupling, the S magnetization is completely antiphase in the transverse plane if the delay period τ is misset at $1/(4J)$ or $3/(4J)$, as in Fig. 1g. Even transients are still represented by Fig. 1a, and so overall the decoupled signal intensity is halved. Ideal on-resonance decoupling, achieved by sampling the signal at integral multiples of T_p, would yield zero S signal from the odd transients, but realistic

sampling rates will reveal the precession of the antiphase S vectors, which repeats cyclically every $2T_p$, as shown in Figs. 1g–1i, and thus produces sidebands at $n/(2T_p)$.

The I vectors are antiphase along the z axis at the start of decoupling, so Eqs. [8] and [9] still apply, but the S-spin magnetization along the x axis during coupling evolution is now detected as $\sin\varphi(t)$ for the precession shown in the figure, due to the initial antiphase orientation of the S vectors. The Fourier-transformed signal will appear in the imaginary channel, in contrast to the real $\cos\varphi(t)$ signal that generates the centerband and regular sidebands, so in an actual NMR experiment, these coherence sidebands will be displayed in dispersion mode if the centerband is phased for absorption mode. The maximum extent of the S-spin precession is shown in Fig. 1h, occurring at $t = T_p/2$, and is repeated in the opposite direction during the second adiabatic inversion. As before, a quick estimate for the peak intensity of the $1/(2T_p)$ dispersion sideband relative to the centerband can be obtained from the amplitude of the sinusoidal modulation. Again, we require a factor of $\frac{1}{2}$ to normalize to a scale where the central peak from the two S-spin vectors has unit intensity, to obtain $0.5\sin(\pi\bar{J}T_p/2)$, which is much larger than the estimate obtained starting with in-phase magnetization. Arguments leading to Eq. [11] allow a better estimate for coherence sidebands by finding the Fourier coefficients of $\sin(\pi\bar{J}t)$, where the signal reverses at $T_p/2$ as before, but has a period $2T_p$ and is an odd function. We obtain

$$B_n = \begin{cases} \dfrac{1}{2}\left[\operatorname{sinc}\dfrac{n-\bar{J}T_p}{2} - \operatorname{sinc}\dfrac{n+\bar{J}T_p}{2}\right] & \text{for } n \text{ odd} \\ 0 & \text{for } n \text{ even} \end{cases}$$

[16]

for the peak-to-peak dispersion-mode amplitude of coherence sidebands at frequency $n/(2T_p)$.

For a typical experimental implementation using $bwdth = 50$ kHz, $T_p = 1$ ms, and $RF_{max} = 9.9$ kHz, actual $1/(2T_p)$ dispersion sidebands for τ misset at $3/(4J)$ are 9.1% of the detected S signal compared to predicted values of 11.0% from $0.5\sin(\pi\bar{J}T_p/2)$, 8.9% given by Eq. [16] and 9.4% from the exact Fourier transformation of $\sin\varphi(t)$. These amplitudes are for the $1/(2T_p)$ sidebands phase-corrected by 90° to be in absorption mode. Sources of error in the measured sideband amplitudes are discussed in the Experimental section. Sideband levels quoted in Ref. *10* were baseline-to-peak amplitude of the dispersion-mode sidebands, which is about half the total amplitude.

Transverse coherence. If transverse coherence terms S_yI_x or S_yI_y are present at the start of decoupling, the I vectors in Fig. 1g would begin in the transverse plane. During an ideal adiabatic inversion pulse, the I vectors would remain spin-locked at 90° with respect to B_e, but would also precess rapidly about this field. The projection of I_α on the z axis, which determines $J_r(t)$ by Eq. [7], thus oscillates rapidly during the pulse, giving rise to a complex pattern of higher-frequency sidebands which we have referred to as sideband noise in our

previous analysis of the problem (*10*). This rapid, short-period oscillation limits the precession amplitude of the S vectors, producing more, but smaller, sidebands compared to the fewer, but larger, sidebands observed for longitudinal coherence S_yI_z.

An easily visualized demonstration of the signals generated by transverse coherence during decoupling is provided by setting $RF_{max} = bwdth/2$. Since $\operatorname{sech}^2(x) + \tanh^2(x) = 1$, the magnitude of B_e is a constant equal to RF_{max} as it is adiabatically rotated from $+z$ through the transverse plane along the x axis to $-z$. We consider the specific case $RF_{max} = 10$ kHz. During an inversion pulse of length $T_p = 1$ ms applied to ^{13}C spins, antiphase magnetization represented by the vectors I_α and I_β, in the transverse plane at the start of the pulse, will execute $RF_{max}T_p = 10$ complete rotations about B_e. As B_e rotates, I_α precesses in the plane orthogonal to B_e, and the projection of I_α along $\pm z$ oscillates with a period $1/RF_{max}$. The vector model therefore predicts that the detected S-spin signal will correspondingly precess and refocus through 10 cycles in 1 ms as $J_r(t)$ oscillates in the manner just described.

The vector model prediction for the signal is also easily calculated. The appropriate expression for $J_r(t)$ could most generally be obtained by transforming to a system rotating about the instantaneous direction of B_e, but it can also be readily visualized in the current example. When B_e has rotated through an angle $\theta(t)$, the plane of the I vectors is tilted at the same angle relative to the x–y plane, as shown in Fig. 4. The two planes share the same y axis, so only the component of I_α along the axis x' in the tilted plane, $(I_\alpha)_{x'}$, has a projection on the z axis. The projection is given by $-(I_\alpha)_{x'}\sin\theta$, where $\sin\theta = B_1/B_e$ is the sech function in Eq. [1] (since $RF_{max} = bwdth/2$), and $(I_\alpha)_{x'}$ is $\cos(2\pi B_e t)$ for S_yI_x coherence at the start of decoupling and $\sin(2\pi B_e t)$ for S_yI_y coherence. The sense of rotation illustrated in Fig. 4 is for nuclei of positive gyromagnetic ratio, and we obtain

$$S_yI_y: \quad J_r(t)/J_0 = -\sin(2\pi B_e t)\operatorname{sech}\beta(1 - 2t/T_p) \qquad [17]$$

for the instantaneous coupling due to the presence of S_yI_y coherence at the start of on-resonance sech/tanh decoupling with B_e of constant magnitude. The time-dependent coupling in this case results from the model I vectors perpendicular to B_e precessing about this field as it rotates in the x–z plane.

The analogous expression for the S_yI_x case would substitute cosine for sine in Eq. [17], but there is an additional nuance that provides further confirmation of the vector model. Since $B_1(0) \propto \operatorname{sech}\beta$ is not equal to zero, $B_e(0)$ has a small x component. The pulse begins slightly tilted with respect to the z axis, and the plane of the I vectors is not exactly orthogonal to B_e. The I-vector component perpendicular to B_e, which generates the high-frequency oscillations in J_r described previously, is $I_\alpha\cos\theta(0) = I_\alpha\tanh\beta$ and is within 0.005% of I_α for $\beta = 5.3$. The component parallel to B_e is $I_\alpha\sin\theta(0) = I_\alpha\operatorname{sech}\beta$, giving a 1% correction for $\beta = 5.3$. This will produce a cos
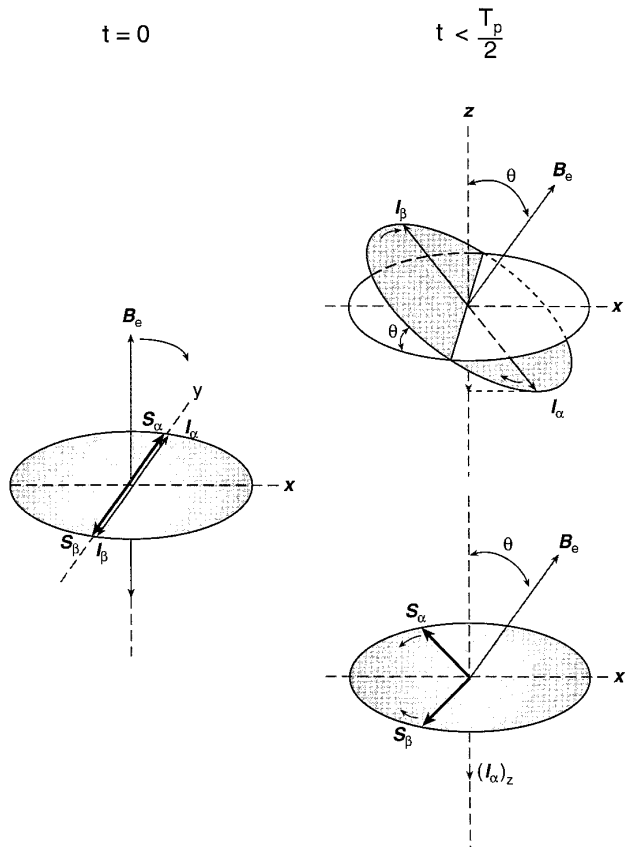
t = 0 $t < \dfrac{T_p}{2}$

FIG. 4. The evolution of observable S-spin magnetization when adiabatic decoupling is applied to transverse coherence S_yI_y is illustrated according to the vector model. The left panel shows the initial configuration of the system, with the I and S vectors aligned with the y axis. The I vectors precess about the decoupling field B_e during the adiabatic sweep, as shown in the upper right panel for an arbitrary time prior to the midpoint of the adiabatic inversion pulse. In the model, the projection of I_α on the z axis determines the instantaneous reduced coupling $J_r(t)$ according to Eq. [7]. The propellar-like motion of I_α in the plane perpendicular to B_e therefore produces a high-frequency oscillation in the coupling, as compared to the examples shown in Fig. 1, resulting in concomitant reversals of the S-spin precession shown in the lower right panel. Predictions of the model are described further in the text and compared with experiment in Fig. 5.

$\theta(t)$ dependence in J_r according to Eq. [3], where $\cos\theta = \Delta H/B_e$ is the tanh function in Eq. [1], and a longer modulation period of T_p compared to the high-frequency oscillations. Since the precession angle $\varphi(t)$ of the S-spin vectors is the integral of the angular frequency $\pi J_r(t)$, the accumulation of phase φ during the low frequency modulation can be a larger fraction of the total phase than might be apparent from considering the magnitude of the sechβ factor alone. The vector model therefore predicts an important distinction between the decoupled signals from S_yI_x and S_yI_y, with an additional modulation of period T_p in the S_yI_x case due to the contribution the I-vector component along B_e makes to J_r, giving

S_yI_x: $\quad J_r(t)/J_0 = -[\cos(2\pi B_e t)\text{sech }\beta(1 - 2t/T_p)]\tanh\beta$
$$+ [\tanh\beta(1 - 2t/T_p)]\text{sech }\beta. \qquad [18]$$

The result of integrating the second term in Eq. [18] to obtain its contribution to the precession angle, φ, has already been considered in the Appendix as the particular case $v = 1$, and the other terms in Eqs. [17] and [18] can be integrated numerically to generate the signal $\sin\varphi(t)$ for antiphase S magnetization at the start of decoupling, as discussed earlier for the S_yI_z case illustrated in Figs. 1g–1i. The results are shown in Fig. 5, where the vector model predictions for the signals resulting from S_yI_x and S_yI_y coherence at the start of decoupling are compared with experiment and the predictions of quantum mechanics. The results are plotted over the course of a single decoupling inversion pulse implemented using a value sech $\beta = 0.02$ to show more clearly the additional low frequency modulation predicted for the S_yI_x signal compared to S_yI_y. The agreement among model, theory, and experiment is evident.

The vector model provides a physical mechanism that simply and accurately predicts the time evolution of observable magnetization when adiabatic decoupling is applied to initial transverse coherence. The model pictures I_α and I_β rotating in propeller fashion about B_e. The magnitude of J_r will be a maximum for the S_yI_x case at time $T_p/2$, when B_e is aligned with the $+x$ axis and the large component of I_α perpendicular to B_e is aligned with $-z$ after completing five rotations in the plane orthogonal to B_e. The smallest oscillations occur near the beginning and end of the pulse, when B_e is close to the z axis and I_α is near the transverse plane. For the S_yI_y case, I_α begins aligned with $+y$, giving $J_r(0) = 0$, and returns to $+y$ at the end of each precession about B_e, since B_e is rotating in the x–z plane. At $T_p/2$, after five such cycles about the effective field, J_r is again zero and the maximum in magnitude for J_r thus occurs a quarter period of the precession cycle earlier, shifting the signal maxima for S_yI_x and S_yI_y relative to each other by the same amount. In addition, since $J_r(0) = 0$ for S_yI_y, the precession amplitude of the S magnetization will be a maximum at each subsequent zero-crossing of J_r, giving a signal that is symmetric about $T_p/2$, as observed. The excellent agreement between theory and experiment in Fig. 5 provides further support for the utility of the model.

Elimination of coherence sidebands. The methods we described to eliminate coherence sidebands (*10*) utilized field gradient pulses to randomize either transverse antiphase I or S magnetization, or both, across the bulk sample. In terms of vectors, randomization of the undesirable components of the S-spin magnetization directly prevents the detection of a net signal, whereas randomization of the I spins insures that the precession of the coupled S spins at any given point in the sample will be cancelled by an equal but opposite precession at some other point of the sample. The bandwidth for these techniques is limited by the bandwidth of the 90° pulses required to convert longitudinal antiphase I magnetization to transverse magnetization, or to preserve transverse in-phase S magnetization along the z axis during the pulsed gradients. Nonetheless, effective decoupled bandwidths of up to 100 kHz
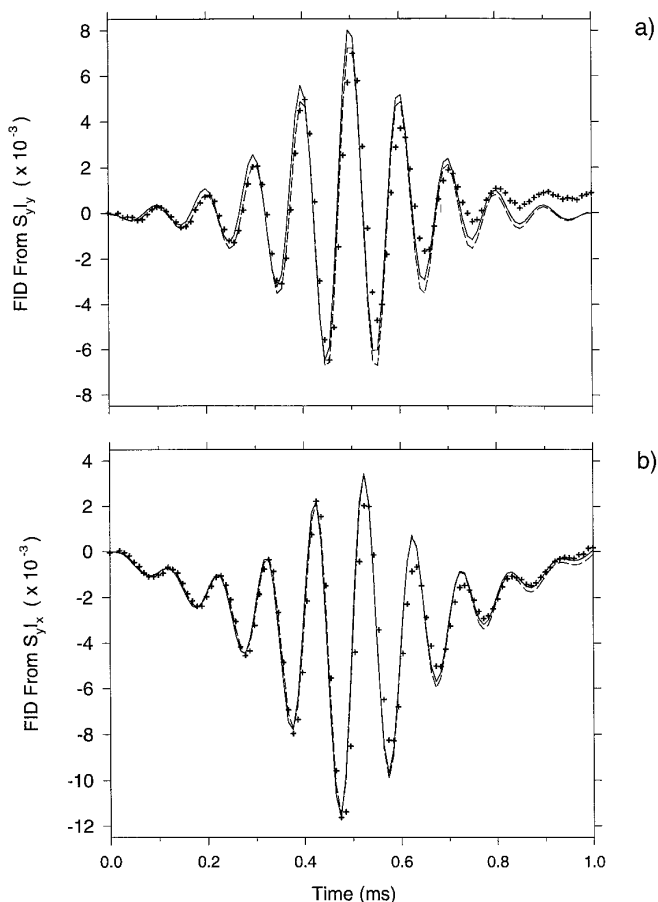
FIG. 5. Signals resulting from the presence of (a) S_yI_y and (b) S_yI_x transverse coherence at the start of a decoupled acquisition are plotted as a function of time during the first inversion pulse of the decoupling sequence. Predictions of the vector model (dashed lines) based on Eqs. [17] and [18] for ideal sech/tanh decoupling applied on resonance to I-spin ^{13}C are compared with experimental data (+) for ^{1}H-detected S spins and quantum-mechanical simulations (solid lines). All FIDs are scaled relative to a signal of unit amplitude from ideally decoupled in-phase magnetization, S_x. A constant-magnitude decoupling field of 10 kHz was generated by setting $RF_{max} = 10$ kHz $= bwdth/2$ in Eqs. [1] and [2] for the implementation of the sech/tanh pulse, chosen to be of length $T_p = 1$ ms. As antiphase I_x or I_y precesses about B_e (see Fig. 4) at the frequency 10 kHz, the projection of the I vectors on the z axis executes 10 complete oscillations during 1 ms as B_e rotates from $+z$ to $-z$ (five cycles of increasing amplitude followed by five of decreasing amplitude). The vector model therefore predicts 10 oscillations in the time-dependent coupling $J_r(t)$, with a corresponding modulation of the S-spin signal. For the S_yI_x case, the plane of the I vectors is not exactly orthogonal to B_e, since $B_1(0) \propto \text{sech}(\beta)$. The I-vector component parallel to B_e produces an additional modulation of period T_p superimposed on the high-frequency oscillations, as shown in the lower panel. The slight mismatch at increasing time between the experimental data and the theoretical predictions may be due to RF inhomogeneity in the sample and/or a slight experimental asymmetry in the delivery of the sech/tanh pulse. Although the signals in this example are relatively small, at the lower RF power levels used in practical decoupling sequences where the pulses are no longer ideally adiabatic, the effects of general antiphase coherence can be an order of magnitude larger than the decoupler modulation of the signal from in-phase magnetization, as shown in Fig. 2 of Ref. *10* illustrating methods for eliminating these coherence effects.

were achieved, sufficient for ^{13}C NMR on a ~2 GHz spectrometer. Analogous randomization methods can be devised using RF inhomogeneity across the sample. For example, a maximum-power adiabatic pulse will cause initial transverse magnetization to rotate through a large angle about B_e, as noted in the preceding paragraph, and this angle will vary across the sample. However the design of NMR probes is toward increased RF homogeneity, so these alternative RF randomization techniques are less efficient than their pulsed-field-gradient counterparts.

Although single-transient methods are preferable, alternative double-transient techniques can be readily demonstrated. Thus, we noted (*10*) that phase cycling a 90[I] pulse as $90_{\pm y}$ just prior to decoupling was equally effective as I-spin randomization. This causes any precession of antiphase S vectors to be in opposite directions depending on the phase of 90[I]. An alternative is to apply two (higher power) adiabatic inversion pulses of length $T_p/2$ at the beginning of half of the transients. Thus, at the end of a period of length T_p, the situation is as in Fig. 1g for these transients, whereas Fig. 1i applies to the other half of the transients, and no net S signal can be observed from the S_yI_z coherence. This method is not limited by the bandwidth of 90° pulses.

The vector model thus provides a straightforward physical explanation for the production of coherence sidebands. All adiabatic decoupling methods will generate sidebands from antiphase S magnetization, since the representations of Figs. 1g–1i are still applicable. Only the form of the function $\varphi(t)$ for the precession angle changes for different adiabatic pulses, leading to modest differences in the amplitude of the resulting coherence sidebands.

Asynchronous Decoupling

In composite pulse decoupling, it is common to desynchronize the decoupling pattern from signal acquisition to allow cycling sidebands to vary in phase between transients and self-cancel. We have noted that this method increases maximum sideband amplitudes for sech/tanh decoupling (*8*). This work can be summarized as follows. As an alternative to random asynchronicity, we undertook a detailed study in which the STUD pattern was shifted in time by known amounts. Advancing the decoupling pattern by $0.5T_p$ inverts the $1/T_p$ sideband. Therefore, summation of two transients with zero and $0.5T_p$ advancement would cancel this sideband. However, when the pattern is advanced by $0.5T_p$, a new sideband is induced at $1/(2T_p)$, even on resonance where regular STUD produces no $1/(2T_p)$ sideband in the high-power limit. Signal-averaging will not cancel this sideband.

An explanation for this new sideband is provided in Figs. 1j to 1l. After a $0.5T_p$ advancement of the STUD pattern, B_e is in the transverse plane and will rotate to the $-z$ axis during the second half of the pulse. According to the vector model, in the absence of coherence between the I and S spins, the quantization axis for the I spins is B_e, so the vectors I_α and I_β will be aligned in the

transverse plane, as shown in Fig. 1j. Thus, the z component of I_α is initially zero, and the instaneous coupling constant, J_r, will also be zero by Eq. [7], but will average to $\bar{J}$ over the first half of the pulse, as before. However, because I_α and I_β are now along $\pm z$ when B_e completes its rotation to $-z$, the coupling precession does not reverse as in Fig. 1b, but continues in the same sense at the same average rate for a second $0.5T_p$ period, during which B_e starts along $+z$ and rotates into the transverse plane, as in Fig. 1k. The precession of the S vectors reverses at the end of this period at time T_p, when I_α (and B_e) return to the transverse plane, shown in Fig. 1l. This net precession is then refocused during the next pulse, cycling every $2T_p$ and yielding $n/(2T_p)$ sidebands. The minimum detectable magnetization, is thus $\cos(\pi \bar{J} T_p)$ and by the former arguments we can expect $1/(2T_p)$ sidebands which are a large fraction of $0.25[1 - \cos(\pi \bar{J} T_p)]$. In the high-power example used previously ($bwdth/(RF_{max})^2 = 0.5$, $bwdth = 50$ kHz, $T_p = 1$ ms), Eq. [10] gives $\bar{J} = 0.94 J_0$, and this formula indicates $1/(2T_p)$ sidebands at the 2.4% level for $J_0 = 150$ Hz.

More accurate estimates of sideband amplitudes in asynchronous decoupling can be obtained from an analysis along the lines of Eqs. [8]–[11]. The lower limit of integration for the net precession angle $\varphi(t)$ in Eq. [A1] is now $T_p/2$. This effectively shifts the functional result of the integration, which is $\alpha(t)$ given in Eq. [9], to the left by $T_p/2$ and subtracts $\alpha(T_p/2)$, since this is the relevant factor for the total phase angle that would have accumulated if the integration had started at $t = 0$. In addition, the factor T_p in Eq. [8] becomes $2T_p$, since the period of the modulation is doubled. Using the functional form for $\alpha(t)$ given in Eq. [9], with the start of asynchronous decoupling defined as the new $t = 0$, Eq. [8] becomes

$$\varphi(t) = \pi J_0 [\alpha(t + T_p/2) - \alpha(T_p/2)] T_p. \qquad [19]$$

Fourier analysis of this modulation for sech/tanh decoupling using the experimental parameters listed earlier predicts $n/(2T_p)$ sideband amplitudes for n equal to 1 through 5 of 2.06, -0.53, 0.21, -0.12, and 0.07% compared to experimental values of 1.98, -0.54, 0.16, -0.12, and 0.07%, respectively. Using Eq. [11] with the appropriate modulation period $2T_p$ instead of T_p gives sideband amplitudes of 1.95, -0.48, 0.21, -0.12, and 0.08%.

A simple two-transient scheme which uses STUD decoupling waveforms advanced by $0T_p$ and $0.5T_p$ therefore gives sidebands of 0.5% at $1/T_p$ and 0% at $1/(2T_p)$ for the first transient and -0.54% at $1/T_p$ and 2.0% at $1/(2T_p)$ for the second. Asynchronous decoupling will thus average the $1/T_p$ sideband to almost zero and the new $1/(2T_p)$ sideband to 1.0%, which is twice the amplitude of the normal $1/T_p$ sideband the method is designed to suppress. Incrementing the decoupler waveform in smaller increments and averaging more transients provides no improvement to this basic result. In addition, $1/(mT_p)$ sidebands, produced at lower power by the phase cycles used in adiabatic decoupling, are also increased when

STUD or STUD+ is applied asynchronously. The method does not work well for adiabatic decoupling, in general.

The vector model also explains why the $1/T_p$ sideband is inverted when the decoupler waveform is advanced by $0.5T_p$. For regular decoupling with no advance of the waveform, the intensity of the $1/T_p$ sideband is given by Eq. [11] with $n = 1$ and a sign of $(-1)^{n+1}$. For the advanced waveform, the same formula applies, but the period is doubled and the $1/T_p$ sideband corresponds to $n = 2$, which has a sign of $(-1)^{n+1}$, as before, and is inverted. A more careful analysis also shows that the magnitudes of the two sidebands are only approximately equal. Writing $\mathrm{sinc}(x)$ in the form $\sin(\pi x)/((\pi x))$, the expressions for the sideband magnitude in the two cases can be shown to be equal to the extent the approximation $\sin(\pi \bar{J} T_p) \approx \pi \bar{J} T_p$ is valid.

Phase-Shifted J-Modulation

Recently, a new signal-averaging technique (26) was shown to reduce sidebands to almost insignificant levels for on-resonance adiabatic decoupling in the high-power limit. A $1/T_p$ sideband at the 2% level in a single transient was less than 0.06% after four transients were averaged, which compares favorably with the performance of continuous-wave decoupling on resonance. The vector model and the Fourier shift theorem provide insight into further implications of the method.

The technique shifts the J-modulation of the signal by a time $kT_p/4$, so, for example, the $k = 2$ acquisition begins as in Fig. 1b. This acquisition still has a period T_p, but is out-of-phase by half a period, or π, with respect to the unshifted acquisition, so averaging the two signals will clearly cancel the $1/T_p$ sideband. More generally, for signal $f(t)$, the Fourier transform $F(\nu) = \tilde{f}(t)$ becomes $\exp(i2\pi\nu\tau)F(\nu) = \tilde{f}(t - \tau)$ when $f(t)$ is shifted by τ, as can be seen by a simple change of variable in the Fourier integral. The on-resonance modulation with simple period T_p produces sidebands at frequencies n/T_p, so shifting the modulation by $\tau = kT_p/4$ gives a phase factor $\exp(ikn\pi/2)$ for the sideband at frequency n/T_p in the kth transient, relative to the phase of the unshifted sideband. Thus, sidebands of order $n < 4$ can be completely canceled by averaging four transients ($k = 0, 1, 2, 3$).

However, off resonance, the vector model shows that the modulation period is $2T_p$, producing sidebands at $n/(2T_p)$, and these sidebands are dominant in linear frequency sweeps as the resonance offset is increased. In this case, the relative phase of the sidebands is $\exp(ikn\pi/4)$, and the $1/(2T_p)$ sideband will not be canceled using four acquisitions. Either eight transients are required, canceling sidebands of order $n < 7$, or a larger shift $kT_p/2$ regains the on-resonance factor $\exp(ikn\pi/2)$ for the relative phase and cancels sidebands of order $n < 4$ upon averaging four transients. In the latter case, the $n = 4$ sideband which is not canceled is now the larger $2/T_p$ sideband rather than the $4/T_p$ sideband remaining for the on-resonance example. Since coherence sidebands produced by $S_y I_z$ terms at the start of decoupling also have period $2T_p$, the same arguments apply.

We note that when sech/tanh decoupling is employed, $1/(2T_p)$ sidebands are small to begin with. At the lower RF power levels relevant to practical decoupling applications, sidebands at $1/(mT_p)$ produced by phase cycling the decoupler become prominent. For typical decoupling phase cycles, $m = 5$, 10, or 20, as discussed earlier. An analysis of these sidebands produced at lower power is beyond the scope of the vector model, since the pulse is no longer ideally adiabatic. Nonetheless, the preceding discussion shows why shifting the phase of the signal and averaging transients cannot simultaneously eliminate $1/(5T_p)$ and $1/(10T_p)$ sidebands in addition to $n/(2T_p)$ sidebands without becoming more intricate. Among the alternative multitransient methods, we have found the "accordion" technique of Starcuk et al. (6) to be effective for routine broadband decoupling, since it reduces levels of all sidebands over the decoupled bandwidth.

CONCLUSIONS

A vector model of adiabatic decoupling has been developed that associates a simple physical picture with the processes occurring during decoupling. The model in effect factors the combined influence of IS coupling, of strength J_0, and the RF irradiation applied to the I spins into two independent operations: (i) The time evolution of a pair of antiphase vectors I_α and I_β defined in the model is determined by the RF field in the usual manner, with components parallel to the effective applied field, B_e, remaining spin-locked along this direction and components perpendicular to B_e precessing about the field. The projection of I_α on the z axis (i.e., defined by the direction of B_0) scales J_0 to produce a time-dependent reduced coupling $J_r(t)$. (ii) The coupling evolution of the S-spin magnetization is determined by $J_r(t)$ instead of J_0. There is almost exact agreement between the vector model and the predictions of quantum mechanics under conditions where $B_e \gg J_0$ (a negligible restriction in many applications) and the adiabatic inversion pulses are close to ideal.

The model can be used with facility to predict the results of decoupling and, in particular, maximum sideband intensity, in a variety of useful applications. The model clearly illuminates the capabilities and limitations of two examples considered as possible methods for reducing sidebands and provides a simple physical mechanism for the phenomenon of coherence sidebands resulting from misset J-delay periods. At the quantum level, coherence sidebands are the signals detected from longitudinal/transverse coherence during decoupling as the time-dependent RF field induces transitions that would otherwise be forbidden in its absence. From the point of view of the vector model, a detectable in-phase component of the S-spin magnetization evolves from the initial antiphase configuration due to changes in coupling induced by the RF field and its action on the I vectors. In the absence of RF irradiation, transverse coherence is undetectable not only because the S magnetization is antiphase, but because the transverse I magnetization results in a coupling of zero. The spins are

truly decoupled and no evolution to detectable magnetization occurs in the S spins.

In the high-power limit $bwdth/(RF_{max})^2 \lesssim 0.5$, where the sech/tanh pulse is ideally adiabatic to a high degree of approximation, we have derived an analytical expression for the time-dependent coupling $J_r(t)$ that is operative during hyperbolic-secant decoupling, both on and off resonance, as a function of the experimental inputs RF_{max}, $bwdth$, and T_p. We have also derived closed-form solutions for the decoupled signal. A simple estimate of the dominant sideband over the full decoupled bandwidth for sech/tanh decoupling can be obtained as $0.25[1 - \cos(\pi \bar{J}T_p/2)]$, where the average coupling $\bar{J}$ given in Eq. [10] is typically greater than $0.9J_0$. A more accurate expression was provided in Eq. [11] that sets limiting values for the central decoupled peak ($n = 0$) and maximum sideband ($n = 1$) in sech/tanh decoupling, as a function of the same experimental inputs. The maximum amplitude of coherence sidebands was also shown to be a large fraction of $\sin(\pi \bar{J}T_p/2)$, with a more accurate expression derived in Eq. [16]. For decoupling methods that employ a linear frequency sweep, maximum sideband intensity was shown to depend sensitively on the resonance offset of the decoupler, with the intensity of the $n = 2$ order sideband quickly surpassing the intensity of the on-resonance $n = 1$ order sideband. The derived limits for sech/tanh decoupling establish simple and accessible criteria for evaluating the performance of potentially superior methods.

Although the pulses are no longer perfectly adiabatic at the lower power levels used in most practical applications of adiabatic decoupling, phase cycles are routinely used to compensate for the decreased performance of the constituent pulses and maintain maximum sideband levels near the ideal limits presented here. However, an additional consideration in these cases is the close relation between sideband and centerband intensities illustrated in Fig. 2, which shows the reduction of the centerband as a function of maximum sideband intensity in the high-power limit. This effect is exacerbated at lower RF power, where total sideband intensity increases and subtracts further from the centerband, despite the success of the phase cycle in keeping maximum sideband levels relatively low. Reduced sideband levels in a single transient translate to increased centerband intensity, while signal-averaging methods that reduce net sideband levels cannot correspondingly increase the centerband, since the centerband intensity is established by the level of sidebands in a single transient. The experimental parameters that enable sech/tanh decoupling to most efficiently approach the ideal performance described here in a single transient are presented in a separate paper in this issue (27).

APPENDIX

Starting with in-phase S magnetization, as in Fig. 1a, the precession angle of S_β in the transverse plane during a single sech/tanh decoupling pulse is obtained by integrating the time-dependent angular frequency, $\pi J_r(t)$, to obtain, through Eq. [3],

$$\varphi(t) = \pi J_0 \int_0^t \cos\theta\,(t')dt', \qquad [A1]$$

where $\cos\theta = \Delta H/B_e$ for θ equal to the polar angle between the effective field $B_e = [B_1^2 + (\Delta H)^2]^{1/2}$ and the z axis. We use Eqs. [1] and [2] and make the substitution $x = \beta(1 - 2t/T_p)$ to write the integrand as

$$\cos\theta = \frac{\dfrac{bwdth}{2}(\tanh x + s)}{\sqrt{RF_{max}^2\,\mathrm{sech}^2 x + \left[\dfrac{bwdth}{2}(\tanh x + s)\right]^2}}. \qquad [A2]$$

Defining $v = RF_{max}/(bwdth/2)$, Eq. [A2] can be rearranged as

$$\cos\theta = \frac{\sinh x + s\cosh x}{\sqrt{v^2 + (\sinh x + s\cosh x)^2}}. \qquad [A3]$$

On resonance ($s = 0$), using $\sinh^2 x = \cosh^2 x - 1$, and defining $\xi^2 = |1 - v^2|$ gives

$$\cos\theta = \frac{\sinh x}{\sqrt{\cosh^2 x - \xi^2}} \qquad [A4]$$

for $v < 1$, which is the relevant domain for practical applications of adiabatic decoupling. Finally, we substitute $u = (1/\xi)\cosh x$. Integrating over x instead of t has also introduced a factor $-T_p/(2\beta)$, and Eq. [A1] becomes

$$\varphi = \pi J_0 \frac{T_p}{2}\frac{1}{\beta}\int \frac{-du}{\sqrt{u^2 - 1}}$$

$$= \pi J_0 \frac{T_p}{2}\frac{1}{\beta}(-\cosh^{-1} u). \qquad [A5]$$

Evaluating $u = |1 - v^2|^{1/2}\cosh\beta(1 - 2t'/T_p)$ from 0 to t gives Eqs. [8] and [9]. If $v > 1$, then the integrand in Eq. [A5] becomes $(u^2 + 1)^{1/2}$ to give $\sinh^{-1} u$, while $v = 1$ gives $\xi = 0$ in Eq. [A5], and the substitution $u = \cosh x$ gives the result $\ln u$ for the integration.

For more general resonance offset s, expanding the hyperbolic functions in Eq. [A3] in terms of their component exponentials gives two terms equal to

$$\pm \frac{(1 \pm s)e^{\pm x}}{\sqrt{4v^2 + [(1 + s)e^x - (1 - s)e^{-x}]^2}}. \qquad [A6]$$

Factoring the denominator as $\exp(\mp x)$ times the appropriately rearranged radical and making the substitution $u = \exp(\pm 2x)$ gives two integrals of the form

$$\frac{1}{2}(1 \pm s)\int \frac{du}{\sqrt{a + bu + cu^2}}, \qquad [A7]$$

which can be found in standard integral tables. These integrals replace the single integral in Eq. [A5], derived for the precession angle φ on resonance, and are evaluated for $u = \exp(\pm 2x)$, with x the same function of time given above. The corresponding constants in each integrand are

$$\begin{aligned} a &= (1 \mp s)^2 \\ b &= 4v^2 - 2(1 - s^2) \\ c &= (1 \pm s)^2 \end{aligned} . \qquad [A8]$$

REFERENCES

1. D. T. Pegg, M. R. Bendall, and D. M. Doddrell, *J. Magn. Reson.* **44**, 238 (1981).
2. M. R. Bendall, D. T. Pegg, and D. M. Doddrell, *J. Magn. Reson.* **45**, 8 (1981).
3. M. R. Bendall, D. T. Pegg, and D. M. Doddrell, *J. Magn. Reson.* **52**, 81 (1983).
4. M. R. Bendall, *J. Magn. Reson. A* **116**, 46 (1995).
5. M. S. Silver, R. J. Joseph, and D. I. Hoult, *J. Magn. Reson.* **59**, 347 (1984).
6. Z. Starčuk, Jr., K. Bartušek, and Z. Starčuk, *J. Magn. Reson. A* **107**, 24 (1994).
7. M. R. Bendall, *J. Magn. Reson. A* **112**, 126 (1995).
8. T. E. Skinner and M. R. Bendall, *J. Magn. Reson.* **124**, 474 (1997).
9. T. E. Skinner and M. R. Bendall, *J. Magn. Reson. A* **123**, 111 (1996).
10. M. R. Bendall and T. E. Skinner, *J. Magn. Reson.* **129**, 30 (1997).
11. M. H. Levitt, G. Bodenhausen, and R. R. Ernst, *J. Magn. Reson.* **53**, 443 (1983).
12. R. E. D. McClung, T. T. Nakashima, and B. K. John, *J. Magn. Reson.* **58**, 173 (1984).
13. A. Bax, G. M. Clore, P. C. Driscoll, A. M. Gronenborn, M. Ikura, and L. E. Kay, *J. Magn. Reson.* **87**, 620 (1990).
14. J. Baum, R. tycko, and A. Pines, *Phys. Rev. A* **32**, 3435 (1985).
15. D. E. Demco, H. Köstler, and R. Kimmich, *J. Magn. Reson. A* **110**, 136 (1994).
16. L. Müller and R. R. Ernst, *Mol. Phys.* **38**, 963 (1979).
17. J. S. Waugh, *J. Magn. Reson.* **49**, 517 (1982).
18. W. A. Anderson and R. Freeman, *J. Chem. Phys.* **37**, 85 (1962).
19. M. R. Bendall, D. T. Pegg, D. M. Doddrell, and J. Field, *J. Amer. Chem. Soc.* **103**, 934 (1981).
20. M. R. Bendall and T. E. Skinner, *J. Magn. Reson. A* **120**, 77 (1996).
21. C. P. Slichter, "Principles of Magnetic Resonance," 3rd ed., p. 306, Springer-Verlag, New York (1990).
22. Ē. Kupče and R. Freeman, *J. Magn. Reson. A* **115**, 273 (1995).
23. R. Fu and G. Bodenhausen, *J. Magn. Reson. A* **117**, 324 (1995).
24. Ē. Kupče and R. Freeman, *J. Magn. Reson. A* **118**, 299 (1996).
25. A. Tannús and M. Garwood, *J. Magn. Reson. A* **120**, 133 (1996).
26. Ē. Kupče and R. Freeman, *J. Magn. Reson.* **127**, 36 (1997).
27. M. R. Bendall and T. E. Skinner, *J. Magn. Reson.* **134**, 331–349 (1998).